3-15-2020

Structure, Wettability, Corrosion and Biocompatibility of Nitinol Treated by Alkaline Hydrothermal and Hydrophobic Functionalization for Cardiovascular Applications

S. Rahimipour
K.N. Toosi University of Technology

E. Salahinejad
K.N.Toosi University of Technology

E. Sharifi
Hamadan University of Medical Sciences

H. Nosrati
Shahrekord University of Medical Sciences

Lobat Tayebi
Marquette University, lobat.tayebi@marquette.edu

Applied Surface Science, Vol. 506 (March 15, 2020): 144657. DOI.

Structure, Wettability, Corrosion and Biocompatibility of Nitinol Treated by Alkaline Hydrothermal and Hydrophobic Functionalization for Cardiovascular Applications

S. Rahimipour
Faculty of Materials Science and Engineering, K. N. Toosi University of Technology, Tehran, Iran
E. Salahinejad
Faculty of Materials Science and Engineering, K. N. Toosi University of Technology, Tehran, Iran
E. Sharifi
Department of Tissue Engineering and Biomaterials, School of Advanced Medical Sciences and Technologies, Hamadan University of Medical Sciences, Hamadan, Iran
H. Nosrati
Department of Tissue Engineering, School of Advanced Technologies, Shahrekord University of Medical Sciences, Shahrekord, Iran

L. Tayebi
Department of Developmental Sciences, Marquette University School of Dentistry, Milwaukee, WI

Abstract
The main objective of this study is to hydrophobize nitinol (Ni-Ti alloy) for cardiovascular applications. For this purpose, medical nitinol samples were subjected to sodium hydroxide hydrothermal treatments at various temperatures, followed by hexadecyltrimethoxysilane (HDTMS) functionalization. Then, the structure, wettability, corrosion, cytocompatibility and cell adhesion of the prepared samples were evaluated. According to the results, porous blade-shaped layers of sodium titanate were formed on the substrate surface as a result of the alkaline treatment. These nano-rough features offered considerable hydrophobicity after HDTMS processing, where a maximum water contact angle of about 140° was obtained for the sample treated at 120 °C, followed by the HDTMS coating. In contrast to the individual application of the alkaline treatments, the subsequent HDTMS processing improved corrosion resistance in the simulated body fluid. Although all the samples presented appropriate cytocompatibility with respect to human umbilical vein endothelial cells, the cells did not show an adhesion tendency to the hydrophobic surfaces. It is concluded that alkaline hydrothermal and HDTMS processed nitinol can be considered for cardiovascular applications demanding hydrophobic surfaces.

Keywords
Nitinol, Alkaline treatment, Hexadecyltrimethoxysilane, Wettability, Corrosion, Biocompatibility

1. Introduction
Nitinol (NiTi) has a variety of applications in different fields, due to its shape-memory effect, superelasticity, relatively low elastic modulus, proper compressive strength, high fatigue strength, considerable corrosion resistance and good biocompatibility. Orthodontic wires [1], bone fracture fixation plates [2], stents [3], [4], blood filters [5], [6], artificial cardiac muscles [7], spacers between spinal vertebrae [8], micro-electro-mechanical biosystems valves [9] and Simon filters [10], [11] are some examples for the medical applications of this alloy. However, the release of ions from this biomaterial can lead to allergic and toxic reactions in the body, as a result of electrochemical corrosion in the environment. Typically, cells are deformed and chromosomes are damaged, due to the exposure of Ni^{2+}. Also, divalent ions like Ca^{2+}, Mg^{2+} and Zn^{2+} are displaced by Ni^{2+} in enzymes and proteins, disadvantageously causing to change their molecular structure [12]. Another challenge for the cardiovascular applications of this alloy is the accumulation of protein and thereby blood coagulation. Thus, anticoagulant drugs like heparin are frequently prescribed along with the use of nitinol implants [13], [14], [15]. Both of these drawbacks can be controlled by hydrophobization of the alloy surface, where the treated surfaces repel fluids and proteins and benefit from higher corrosion resistance and hemocompatibility [16], [17].

Superhydrophobic surfaces are demanded in daily life and industrial applications. The typical applications of these surfaces are self-cleaning [18], water-resistant surfaces [19], anti-fogging surfaces [20], anti-icing surfaces [21], anti-corrosion surfaces [22], preventing the loss of fluid [23], and

so on. It has been proved that superhydrophobic surfaces can be achieved by depositing low surface energy substances along with increasing the surface roughness [24]. By studying natural creatures, including lotus leaves and butterfly wings, it has been confirmed that special hierarchical structures—due to the inherent roughness of micro-scale and nano-scale— play a major role in water repellency [25], [26]. Due to this phenomenon, dual synthetic roughness is widely used in the development of superhydrophobic surfaces.

This work aims to hydrophobize nitinol while keeping or improving biocompatibility for cardiovascular applications. To do so, nitinol surfaces were roughened by alkaline hydrothermal treatment and reduced in surface free energy by depositing an alkoxysilane material, namely hexadecyltrimethoxysilane (HDTMS), for the first time. In comparison to other routes used particularly to construct TiO_2 nanostructures with high biocompatibility, controllable wettability and adhesion [27], [28], [29], the alkaline treatment is a more simple, flexible and inexpensive method which forms a layer of alkali compounds on the surface. HDTMS is a substance with low surface energy due to its long hydrocarbon chains [30]. In contrast to fluorine-containing silane compounds, HDTMS is environmentally friendly and has been used to hydrophobize various materials, including metals and alloys, fabrics, membranes, etc. [31], [32], [33]. It has been reported that the alkaline treatment of titanium-based alloys results in the reduction of cells cytocompatibility and proliferation due to the local increase of pH and Ni^{2+} release [29], [34], [35]. On the contrary, this surface processing enhances apatite-formation ability [35], [36], [37] and cell adhesion due to the alteration of roughness, wettability and bioactivity [35], [38]. In this regard, reverse influences have been reported as a result of surface hydrophobization, where the adhesion of vitronectin and fibronectin proteins is roughness and wettability dependent [39], [40], [41].

2. Experimental procedures

2.1. Pretreatment

Medical-grade nitinol (NiTi, Kellogg's Research Labs, US) disks of 8 mm in diameter were first polished by sandpapers to 600 grits. They were then washed in acetone, ethanol and distilled water under ultrasonication. The samples obtained from this processing were assigned as the pretreated samples.

2.2. Alkaline hydrothermal treatment

The pretreated samples were exposed to a 10 M NaOH (Merck, Germany, 99.0%) aqueous solution at 60, 120 and 180 °C for 48 h. Afterwards, the alkaline-treated samples were washed in distilled water and subsequently dried at 80 °C for 2 h.

2.3. HDTMS functionalization

A mixture of 90 ml of ethanol and 10 ml of distilled water was first loaded with 3 wt% HDTMS ($H_3C(CH_2)_{15}Si(OCH_3)_3$, Sigma-Aldrich). While magnetic stirring, acetic acid was dropwise added to adjust the pH to about 5. The pretreated and alkaline-treated samples were soaked in this HDTMS solution for 2 h. Then, the samples were rinsed with ethanol and distilled water and dried at 120° C for 1 h. The codes assigned to the samples treated with the different processing approaches are listed in Table 1.

Table 1. Sample coding, as a function of the alkaline treatment temperature and HDTMS coating.

Specification	**Sample Code**							
	1	**2**	**3**	**4**	**5**	**6**	**7**	**8**
Alkaline Treatment Temperature (°C)	–	60	120	180	–	60	120	180
HDTMS Coating	–	–	–	–	✔	✔	✔	✔

2.4. Structural characterization

The processed surfaces were characterized by field emission scanning electron microscopy (FESEM, Mira3 Tescan-XMU) equipped with energy-dispersive X-ray spectroscopy (EDS) at an acceleration voltage of 10 kV and atomic force microscopy (AFM, Park Scientific Instruments-Cp Auto Probe) in terms of morphology, composition and roughness. X-ray diffraction (XRD, PHILIPS-PW1730) was also used for the phase analysis of the samples with a step size of 0.05° and a step time of 2 sec.

2.5. Wettability studies

Five microliters of distilled water were dropped on three different points of the surfaces and photographed by a professional digital camera from side views. The sessile water contact angles were measured by tangent lines to the interfaces at the three-phase points and averages were assigned to each sample.

2.6. Corrosion tests

The samples were first immersed in the Ringer's simulated body fluid for 1 h to obtain steady-state conditions. Electrochemical tests were performed by a Vertex potentiostat/galvanostat device, using a platinum counter electrode and Ag/AgCl reference electrode. Electrochemical impedance spectroscopy (EIS) experiments were run in a frequency range of 10 kHz to 10 mHz with the potential amplitude of 10 mV at the open circuit potential (OCP). Then, polarization tests were conducted at a scan rate of 0.1 mV/s at a potential range of −1 V to +1 V.

2.7. Biocompatibility

The prepared samples were first sterilized in ethanol and then rinsed with the phosphate-buffered saline. Approximately 1.0×10^4 human umbilical vein endothelial cells (HUVECs) were cultured on the samples in the Dulbecco's modified Eagle medium containing 20% fetal bovine serum and 1% antibiotics penicillin and streptomycin for 1, 3 and 7 days in a 48-well plate. Cell counting kit-8 (CCK-8) was used to measure living cells with three repetitions, according to Ref. [42]. To do so, 18 µl of the CCK-8 solution were added to each well and the contents of each well were transferred to a 96-well plate pit after 4 h. Produced colors were analyzed by a plate reader at a wavelength of 450 nm. For statistical analyses, the one-way variance analysis was conducted with *P* value less than 0.05 as the significant level. In addition, the cells cultured on the samples for 1 day were observed by a scanning electron microscope (SEM) after fixing with glutaraldehyde 2.5% (v/v) followed by dehydrating with ethanol solutions (30, 40, 50, 60, 70, 80, 90 and 100%) and coating with gold.

3. Results and discussion

3.1. Structural analyses

In this work, the main aim of using the alkaline treatment process was to control the surface morphology and roughness of nitinol for cardiovascular applications. According to the literature [43], [44], [45], the effect of the alkaline treatment temperature on the surface morphology is more than other process variables. Thus, with the criterion of the changed morphology, the optimal concentration and duration of 10 M and 48 h, respectively, were kept fixed and the effect of the treatment temperature (60, 120 and 180 °C) was assessed. The structural analyses were only conducted on the pretreated and alkaline-treated samples since the molecular-thickness coating of HDTMS does not affect the surface morphology and roughness [31], [46].

Fig. 1 shows the FESEM micrographs and EDS profiles of these samples. As seen, in comparison to the pretreated sample, the alkaline treatment entirely changes the surface morphology with a meaningful dependency on the alkaline treatment temperature. Typically, as a result of the alkaline treatment at 60 °C, some uniform blades of about 100 nm in length and of almost 15 nm in thickness appear on the surface. By increasing the temperature to 120 °C, the number, length and thickness of blades increase, while the blades are still unconnected. Nonetheless, the alkaline treatment at 180 °C declines the spacing of blades and develops a compact arrangement of blades on the surface. The quantitative results of the EDS analyses are also listed in Table 2. The enhancement in the EDS concentration of Na and O by increasing the alkaline treatment temperature is indicative of the morphological growth of the surface layers. Also, the slower decrease of the concentration of Ti in comparison to Ni is an evidence for the presence of titanium in the surface scales. It should be noted that the alkaline treatment temperature, by controlling the nucleation and growth kinetics of the formed surface layers, determines the surface morphology [43], [47].

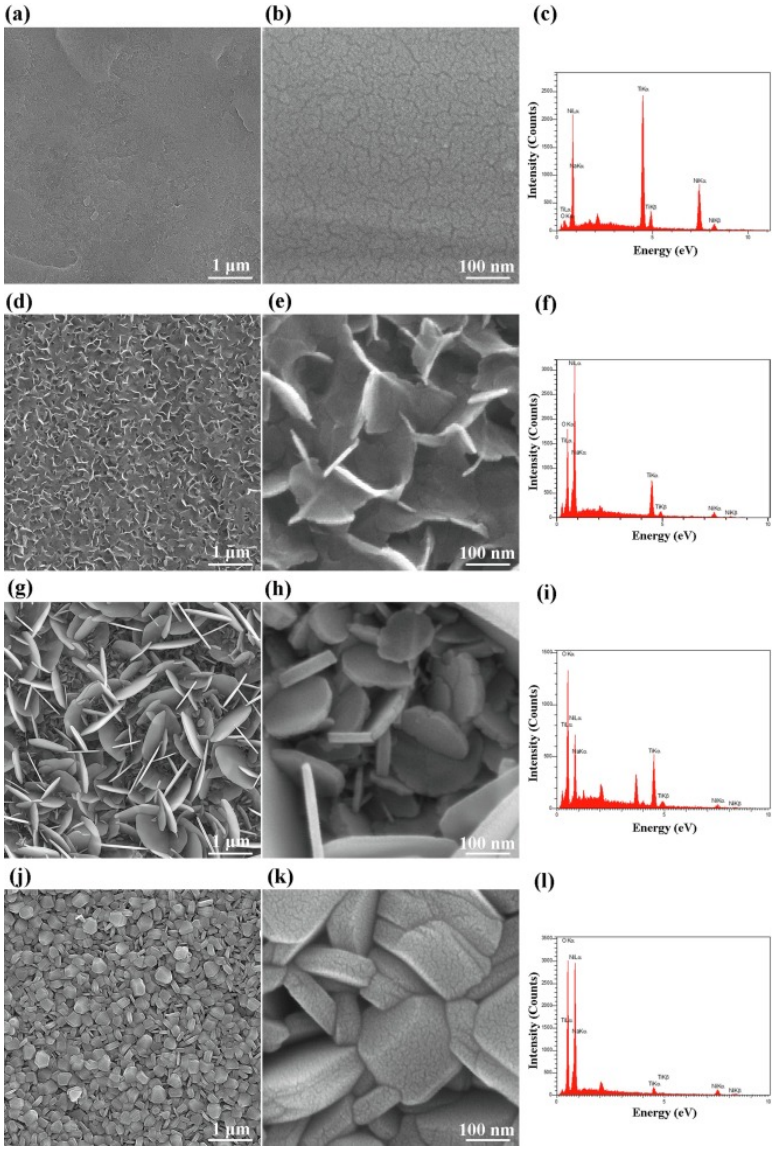

Fig. 1. FESEM micrographs (in two magnifications) and EDS profiles of Samples 1 (a, b and c), 2 (d, e and f), 3 (g, h and i) and 4 (j, k and l), respectively.

Table 2. EDS analysis results on the pretreated and alkali-treated surfaces.

Sample Code	**Element (wt.%)**			
	Ti	**Ni**	**Na**	**O**
1	47.3	47.8	0.0	4.9
2	41.7	37.6	1.2	19.5
3	37.4	28.4	3.3	30.9
4	30.5	18.4	5.2	45.9

The AFM two-dimensional, three-dimensional and height histogram profiles of the samples are presented in Fig. 2. The pretreated surface merely exhibits parallel grooves of polishing. In contrast, regular and uniform projections are observed on the surface of the alkaline-treated samples, with a dependency of the size and density of projections on the alkaline treatment temperature. Roughness

parameters extracted from the AFM analysis are listed in Table 3. According to this table, all the roughness parameters are enhanced from Sample 1 to Sample 2 and then to Sample 3, but they all decrease for Sample 4. Typically, the alkaline treatment increases the level of roughness with respect to the pretreated sample, due to the development of surface scales. The increase of roughness by increasing the alkaline treatment temperature from 60 °C to 120 °C is also attributed to the growth of surface blades; however, its decrease at 180 °C is due to the compression of surface scales, which is in good agreement with the FESEM micrographs (Fig. 1).

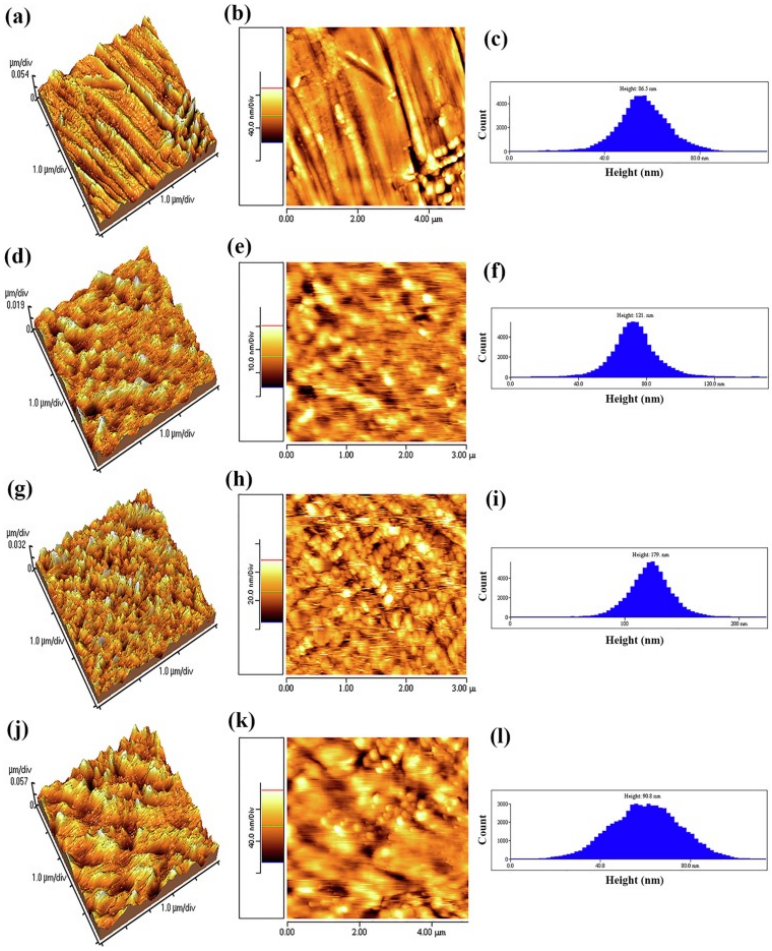

Fig. 2. AFM 3D, 2D, height histogram images of Samples 1 (a, b and c), 2 (d, e and f), 3 (g, h and i) and 4 (j, k and l), respectively.

Table 3. AFM roughness parameters of the pretreated and alkali-treated surfaces (all data is in nanometers).

Sample Code	Average Roughness	Root Mean Square Roughness	Height Difference of Ups and Downs	Mean Height
1	8.40	11.09	108.1	56.05
2	10.87	15.33	150.9	72.83
3	14.69	19.69	223.8	122.00
4	12.27	15.29	113.5	60.03

Fig. 3 depicts the XRD pattern of the pretreated and alkaline-treated samples. In compatible with the EDS analyses, diffraction peaks of NiTi (B2 and B19', the different crystalline phases of nitinol) and $NaTiO_2$ phases are detected in the XRD data. The most typical peak for the four samples belongs to the substrate phase, i.e. NiTi (B2). The three alkaline-treated surfaces are also associated with sodium titanate ($NaTiO_2$), which is in agreement with the literature [48], [49], [50], [51]. The formation mechanism of this phase is also well-established in the literature [48], [49].

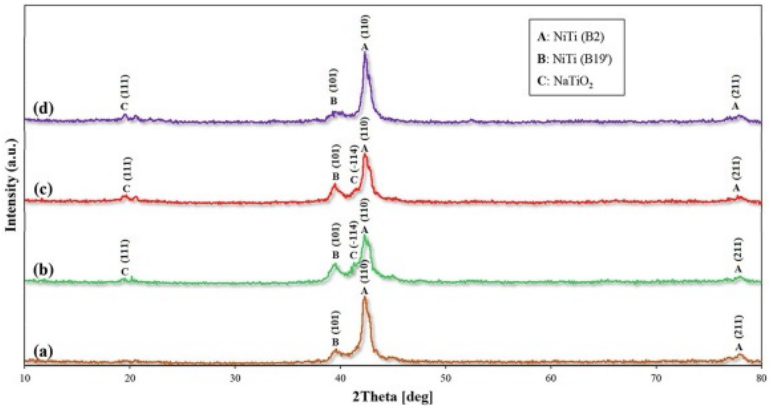

Fig. 3. XRD pattern of Samples 1 (a), 2 (b), 3 (c) and 4 (d).

3.2. Wettability studies

Fig. 4 indicates the side-view macrograph of the water drops on the samples and the quantitative results of the contact angle measurements. It can be seen that Samples 1, 2, 3 and 4 are hydrophilic, while Samples 5, 6, 7 and 8 are hydrophobic. Concerning the hydrophilic surfaces, it is realized that the alkaline treatment decreases the water contact angle, which means the improvement of wettability. This is owing to both the enhancement of roughness and the formation of sodium titanate layers. The latter is accompanied by the formation of a gel layer and hydroxyl groups when exposed to water [34], [52], increasing the surface free energy [53]. For the three alkaline-treated samples, a meaningful enhancement of hydrophilicity is also observed by increasing roughness characterized in Fig. 1, Fig. 2. This is compatible with the Venzel's model [54] in terms of the direct relation of roughness and hydrophilicity. Typically, Sample 3— which is alkaline-treated at 120 °C— presents the highest roughness and wettability with a water contact angle of about 40°.

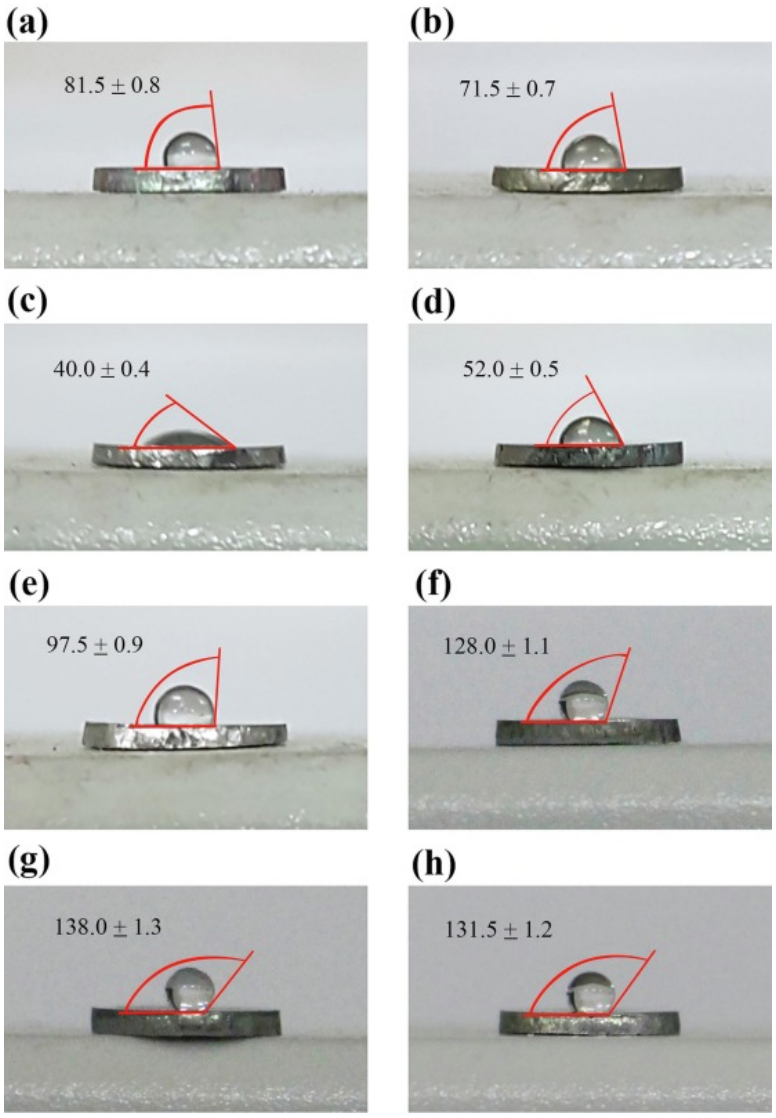

Fig. 4. Macrographs of water drops on Samples 1 (a), 2 (b), 3 (c), 4 (d), 5 (e), 6 (f), 7 (g) and 8 (h).

Essentially, wettability is controlled by both surface free energy and roughness. Thus, the hydrophobicity of the HDTMS-coated samples is attributed to the reduction of the surface energy since the molecular-thickness HDTMS coating does not change the roughness of the pretreated and alkaline-treated substrates. Considering the fact that the roughness of Samples 5, 6, 7 and 8 is proportional to that of Samples 1, 2, 3 and 4, respectively, it is seen that the water contact angle is enhanced by increasing the surface roughness, in good agreement with the Venzel's model [54]. In fact, the water droplet cannot easily penetrate into the cavities of the HDTMS-coated samples and some air remains inside them, because the surface energy is low and thereby the surface repels the water drop [55], [56], [57]. Typically, the alkaline treatment at 120 °C not only yields the highest hydrophilicity, but also offers the highest hydrophobicity after the HDTMS coating. Another noticeable point is that the alkaline treatment provides a suitable platform for HDTMS to ensure its efficiency towards hydrophilicity, since the direct coating of HDTMS on metallic surfaces does not give rise to substantial hydrophilicity [31], [58].

3.3. Corrosion characterization

The *OCP* vs. time curve of the samples is demonstrated in Fig. 5. As can be observed, the *OCP* of Samples 1 and 2 is reduced with time, which is attributed to the lack of a surface protective layer and thereby dissolution. It should be noted that Sample 1 is covered by a passive film after a short period of time, providing a constant *OCP*. On the contrary, the other six samples exhibit relatively constant potentials, due to the balance between the surfaces and electrolyte, where Samples 3 and 4 are protected by full-fledged sodium titanate films (Fig. 1) and the hydrophobic surfaces (Samples 5, 6, 7 and 8) repel the electrolyte. Minor complexities observed in the *OCP*-time curves is also attributed to the surface roughness [59]. It is noticeable that after the period shown in Fig. 5, *OCP* reaches almost constant values.

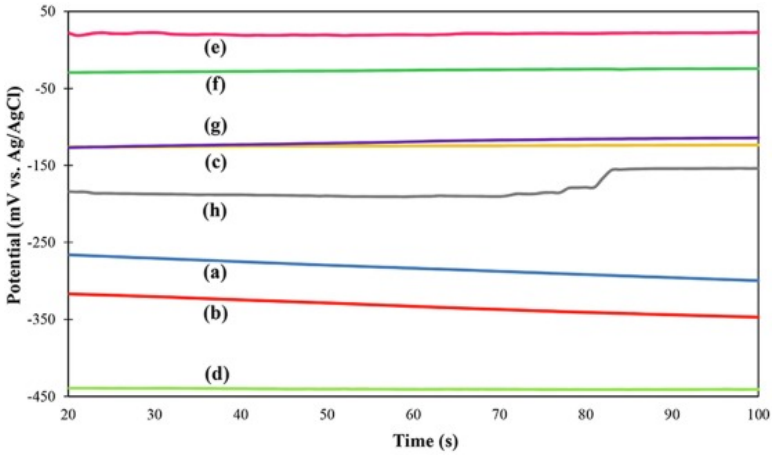

Fig. 5. Electrochemical OCP-time curves of Samples 1 (a), 2 (b), 3 (c), 4 (d), 5 (e), 6 (f), 7 (g) and 8 (h).

The potentiodynamic polarization profiles of the samples, in terms of potential (*E*) vs. current density (*i*), are shown in Fig. 6. The qualitative analysis of the diagrams infers that those of the hydrophobic HDTMS-coated samples are shifted to the left, i.e. smaller current densities, with respect to the hydrophilic samples. This means the improvement of the corrosion resistance in the simulated body fluid, as a result of the liquid repulsion and the reduced actual contact area of the liquid and surface. Table 4 tabulates the electrochemical data extracted from the potentiodynamic polarization diagrams. Typically, Sample 1 represents a lower corrosion current density and rate in comparison to Samples 2, 3 and 4, because the passive layer formed on the surface of the pretreated sample has a higher corrosion resistance than the gel layers existing on the alkaline-treated samples when exposed to the electrolyte [53]. Regarding the HDTMS-coated samples, it is observed that the alkaline treatments at the different temperatures prior to the HDTMS coating yield higher corrosion resistances than the sample which has been only polished prior to coating, as a result of the higher hydrophobicity (Fig. 4). The highest corrosion resistance is also associated with Sample 8 taking advantage of both a high level of hydrophobicity (Fig. 4) and the highest compression level of the sodium titanate alkaline-treated layer (Fig. 1, Fig. 2), via hindering the access of the electrolyte to the metallic nitinol substrate.

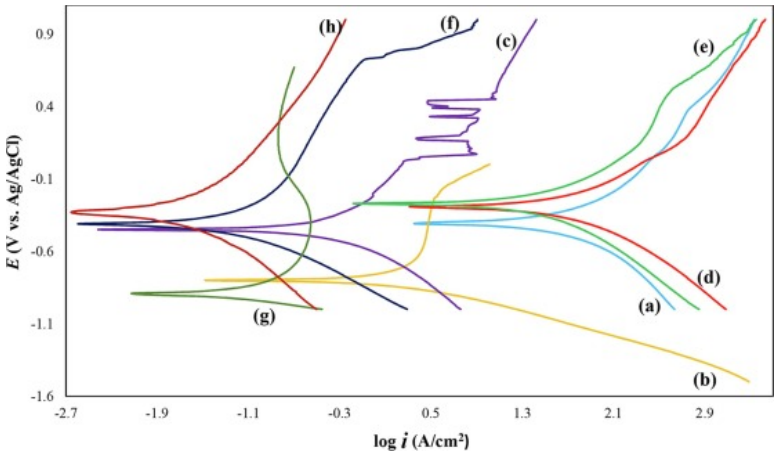

Fig. 6. Potentiodynamic polarization curves of Samples 1 (a), 2 (b), 3 (c), 4 (d), 5 (e), 6 (f), 7 (g) and 8 (h).

Table 4. Corrosion potential ($E_{cor.}$), corrosion current density ($i_{cor.}$), anodic curve slope (β_a), cathodic curve slope (β_c) and polarization resistance (R_p) of the samples.

Sample Code	$E_{cor.}$ (V)	$i_{cor.}$ (A/cm^2)	β_a (V/dec)	β_c (V/dec)	R_p (Ohm.cm^2)
1	−0.4838	8.232E-5	0.975	0.659	2.074E3
2	−0.8033	2.229E-4	3.328	0.219	3.899E2
3	−0.6298	1.263E-4	1.296	0.508	1.254E3
4	−0.4801	1.509E-4	1.190	0.529	1.054E3
5	−0.3784	5.871E-5	0.995	0.567	2.669E3
6	−0.4553	8.983E-8	1.295	0.401	1.480E5
7	−1.0197	5.900E-7	1.926	0.099	2.617E5
8	−0.3738	3.106E-8	0.991	0.602	5.238E5

Fig. 7 illustrates the EIS results of the samples in the simulated body fluid. As observed in Fig. 7a, the Nyquist plots of the samples can be divided into two groups: Samples 1, 2, 5 and 6 with only a semicircular arc and Samples 3, 4, 7 and 8 with two semicircles. Considering the fact that the higher radius of Nyquist semicircular arcs is essentially equivalent to higher corrosion resistance [60], the following corrosion resistance conclusions can be qualitatively drawn from the Nyquist analysis. For the first category of the samples, the alkaline treatment at 60 °C offers a lower corrosion resistance than the pretreated sample, because of the protection difference of the gel and passive films, respectively. Comparing the semicircular arc radius of Samples 1 and 2 with Sample 5 and 6, it can be also found that hydrophobization improves the corrosion resistance due to the electrolyte repulsion, which additionally explains the higher corrosion resistance of Sample 6 than Sample 5. For the second category of the samples, the same upward trend with hydrophobization continues, where Sample 8 with an infinite radius of the second arc presents the highest corrosion resistance in agreement with the polarization results. The Bode impedance plots of the samples (Fig. 7b) also confirms the above-described corrosion resistance ranking since impedance values at low frequencies are a measure of corrosion resistance. The number of the Nyquist semicircular arcs in the two categories of the samples is equal to the number of time constants detected in the Bode phase angle curves (Fig. 7c), where each time constant is indicative of an individual capacitive behavior [61], [62].

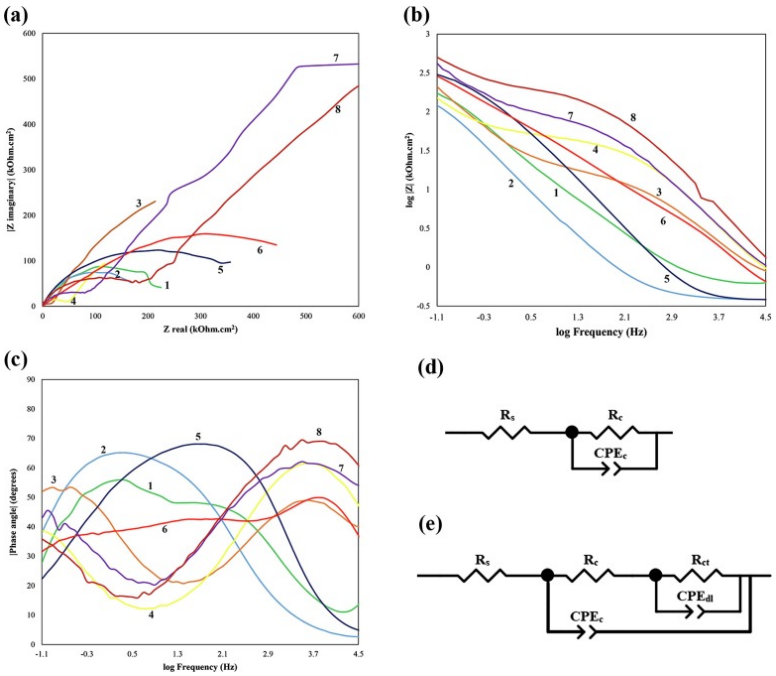

Fig. 7. EIS Nyquist (a), Bode impedance value (b), Bode phase angle (c) and modeling equivalent circuits (d and e) plots of the samples.

In accordance to the qualitative analysis of the Nyquist and Bode plots above, equivalent circuits of Fig. 7d and 7e were used to model the first and second categories of the sample, respectively. In these circuits, constant phase element (CPE) were used instead of capacitors, because the maximum of the Bode phase angle curves deviates from the ideal value of 90°. The impedance of CPEs is calculated by [63]:(1)ZCPE=1Y∞(jω)nwhere Y_0 and n are constants, ω is angular frequency and j is -1. In these circuits, R_s is the electrolyte resistance outside the pores, R_{ct} the charge transfer resistances, R_c is the electrolyte resistance inside the pores and CPE_{dl} and CPE_c are the related elements of double layer and surface scales, respectively. The equivalent capacitance amounts of the CPEs were also calculated by the following equation [39]:(2)C=(Y0·R1-n)1n

The fitting parameters of the EIS results with the proposed circuits are listed in Table 4. Considering the fact that the resistivity (R_{ct} and R_c) and capacitance (C_{dl} and C_c) are in direct and inverse proportion to the corrosion resistance, respectively, it is found that the corrosion resistance ranking of the samples realized from the EIS analysis is compatible with the polarization assessments. That is, the alkaline treatment reduces the corrosion resistance of nitinol; nevertheless, the hydrophobization process enhances it (Table 5).

Table 5. Fitting parameters of the impedance data with the proposed equivalent circuits.

Sample Code	R_s (Ωcm^2)	R_c (KΩcm^2)	$Y_{0(c)}$ (μΩ^{-1}cm^{-2})	n_c	C_c (μF cm^{-2})	R_{ct} (MΩcm^2)	$Y_{0(dl)}$ (μΩ^{-1}cm^{-2})	n_{dl}	C_{dl} (μF cm^{-2})
1	12.66	370.68	1.01	0.89	4.93	–	–	–	–
2	12.70	359.23	1.12	0.88	6.50	–	–	–	–
3	12.82	290.51	1.31	0.86	10.61	2.51	2.76	0.77	304.93
4	12.90	301.21	1.23	0.87	8.36	2.68	2.64	0.79	174.75
5	12.89	410.59	0.88	0.90	3.65	–	–	–	–
6	12.81	427.39	0.81	0.91	2.86	–	–	–	–
7	13.01	451.44	0.69	0.93	1.79	3.07	2.09	0.82	65.23
8	12.88	469.76	0.66	0.93	1.71	3.18	2.03	0.84	40.24

3.4. Biocompatibility assessments

Fig. 8 displays the results of viable cells counting on the prepared and control (C) samples after 1, 3 and 7 days of cell culture, in terms of optical density and cell viability with respect to the control. As can be seen, the optical density values for all the samples are comparable with the control; therefore, the HUVEC viability percentages on the samples are significant and above 85%, which suggests their non-toxicity. The increase in the optical densities with the culture time is also indicative of cell proliferation. Considering the significant level of 0.05 in the variance analysis, the alkaline treatment (Samples 2, 3 and 5) is found to reduce the cell viability in comparison to the pretreated sample (Sample 1). This is attributed, on the one hand, to the reduction in the corrosion resistance (Fig. 6, Fig. 7), which is accompanied by the more release of toxic ions like nickel with a destructive effect on the survival and proliferation of cells [34]. On the other hand, the release of Na^+ incorporated in the alkaline-treated surfaces causes a local enhancement in pH via the exchange with H^+ of the cell medium, which is deteriorous for cells [29], [35]. Thus, the improvement in the cell viability after hydrophobization (Samples 5, 6, 7 and 8) can be explained by the increase in the corrosion resistance (Fig. 6, Fig. 7) and thereby the control of the toxic ions release.

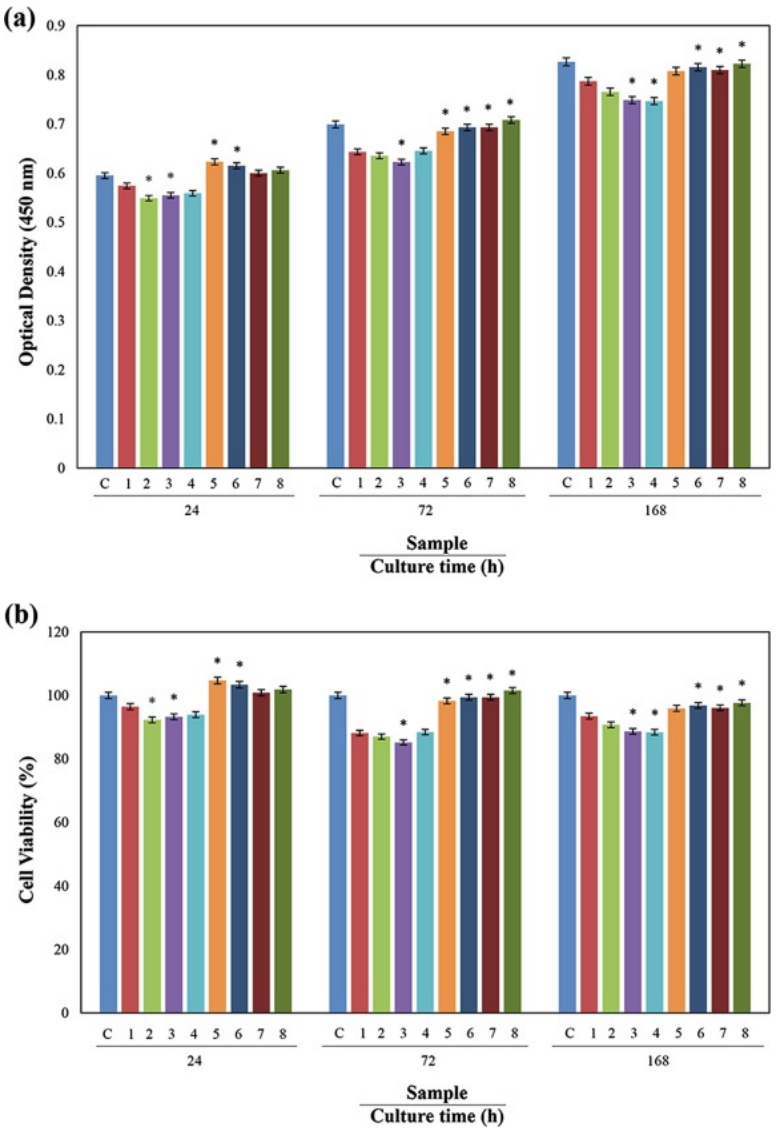

Fig. 8. Spectrophotometer optical density of viable cells (a) and cell viability (b) cultured on the samples. * indicates a significant difference with respect to Sample 1.

To assess the ability of the cell adhesion on the surfaces, the morphology of the cultured cells was analyzed by SEM (Fig. 9). In terms of wide and flat cell spreading with anchored tentacles, the pretreated sample presents a relatively proper cell adhesion feature. The cell adhesion is improved as a result of the alkaline treatments, due to the evolution of roughness (Fig. 1, Fig. 2), wettability (Fig. 4) and bioactivity. The positive contribution of nano roughness and hydrophilicity of biomaterials to the adhesion and proliferation of cells with an encouraging influence on proteins is well established [64], [65], [66], [67]. In addition, some studies have concluded that alkaline-treated titanium-based alloys benefit from a significant level of bioactivity and thereby suitable cell adhesion because of the high biocompatibility of hydroxyapatite [38], [51], [68]. Thus, for these samples, it is inferred that the deteriorous effect of the alkaline treatment on pH and corrosion resistance is not dominant from the viewpoint of the cell adhesion. For the HDTMS-coated samples, Sample 5 represents a partial flattening feature of cell spreading; however, the number of detectable cells and cells spreading are reduced by increasing hydrophobicity (Samples 6, 7 and 8). This suggests the essential effect of wetting on cell adhesion in comparison to the corrosion characteristics, in agreement with Ref. [39]. It would be worth mentioning that these cell adhesion features are compatible with other hydrophobic surfaces [40], [41]. Indeed, the early stages of cell adhesion are essentially affected by vitronectin and fibronectin. The adsorption of these proteins on surfaces strongly depends on the roughness and wettability of the surfaces, whereas some proteins like albumin (an anti-adhesion protein for cells) tend to hydrophobic surfaces [16]. Anyway, hydrophobicity and low cellular adhesion are promising for cardiovascular applications, because of the reduced probability of clotting and blood coagulation [69].

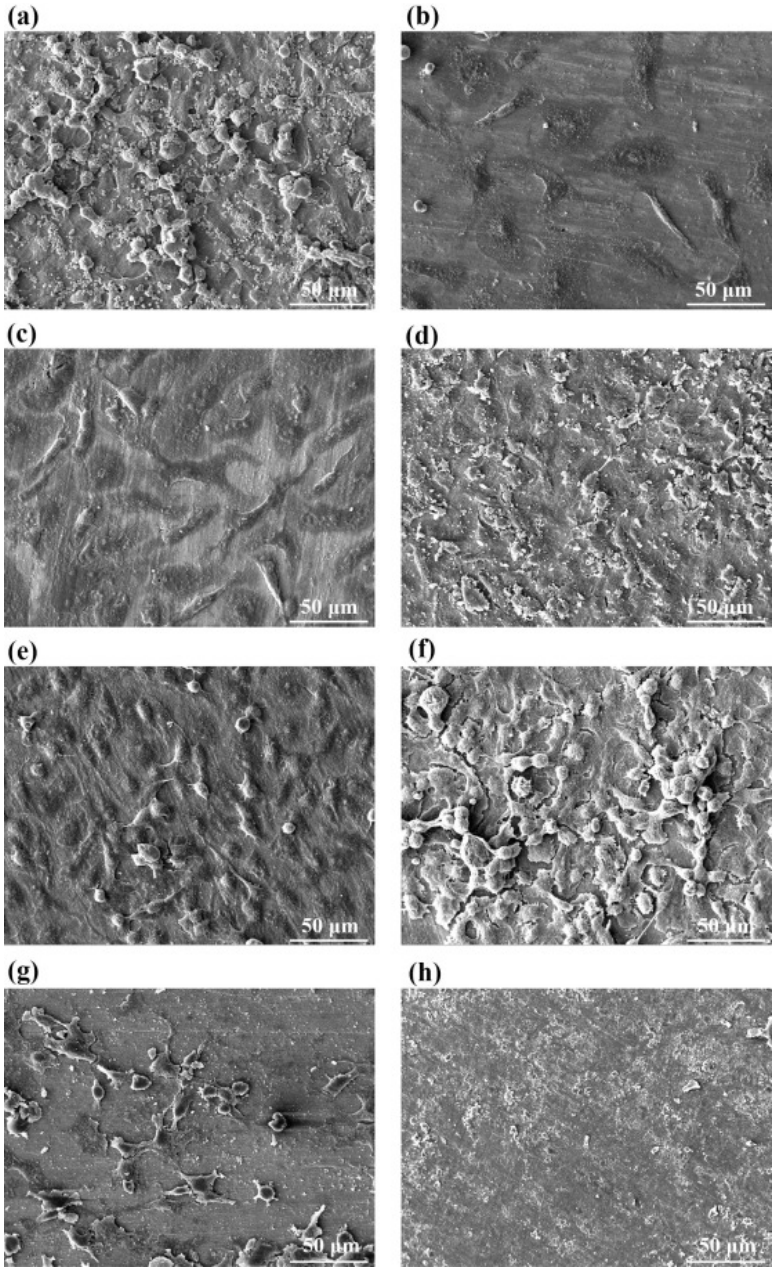

Fig. 9. SEM images of cells fixed on Samples 1 (a), 2 (b), 3 (c), 4 (d), 5 (e), 6 (f), 7 (g) and 8 (h).

4. Conclusions

In this research, the effect of alkaline treatment and HDTMS coating on the structure, wettability, corrosion and biocompatibility of nitinol was studied. The findings of this research are summarized as follows:

1) The morphology of the alkaline-treated surfaces included blades with an increasing tendency to size and compression by enhancing the alkaline treatment temperature.
2) The alkaline treatment increased the surface roughness, with the maximum roughness obtained for the sample treated at 120 °C.
3) The alkaline treatment developed a layer of sodium titanate ($NaTiO_2$) on the nitinol surface.

4) The alkaline treatment increased wettability, but the subsequent HDTMS processing induced hydrophobicity. The highest wettability angle of 138.0 ± 1.3° was obtained for the sample treated at 120 °C followed by the HDTMS functionalization.
5) The alkaline treatment reduced, but HDTMS hydrophobization improved the corrosion resistance, where the sample treated at 180 °C showed the highest corrosion resistance.
6) All of the alkaline hydrothermal and hydrophobic functionalized samples were cytocompatible (non-toxic) with respect to HUVECs.
7) The cell adhesion was improved after the alkaline treatments, but declined by hydrophobization, which can be advantageous for vascular applications.

Author contribution

Saeed Rahimipour: Student-Experiment- Paper writing.
Erfan Salahinejad: Supervisor-Conducting the research- Paper writing.
Esmaeel Sharifi: Collaborator- Cell parts- Paper writing.
Hamed Nosrati: Collaborator- Cell parts- Paper writing.
Lobat Tayebi: Collaborator- Research Idea- Paper writing.

Declaration of Competing Interest

None.

References

[1] M. Arndt, A. Brück, T. Scully, A. Jäger, C. Bourauel. **Nickel ion release from orthodontic NiTi wires under simulation of realistic in-situ conditions.** J. Mater. Sci., 40 (2005), pp. 3659-3667

[2] D. Tarniţă, D. Tarniţă, L. Hacman, C. Copiluş, C. Berceanu. **In vitro experiment of the modular orthopedic plate based on Nitinol, used for human radius bone fractures.** Rom. J. Morphol. Embryol., 51 (2010), pp. 315-320

[3] F. Whitcher. **Simulation of in vivo loading conditions of nitinol vascular stent structures.** Comput. Struct., 64 (1997), pp. 1005-1011

[4] K. Maleckis, E. Anttila, P. Aylward, W. Poulson, A. Desyatova, J. MacTaggart, A. Kamenskiy. **Nitinol stents in the femoropopliteal artery: a mechanical perspective on material, design, and performance.** Ann. Biomed. Eng., 46 (2018), pp. 684-704

[5] M.R. Prince, E.W. Salzman, F.J. Schoen, A.M. Palestrant, M. Simon. **Local intravascular effects of the nitinol wire blood clot filter.** Invest. Radiol., 23 (1988), pp. 294-300

[6] Q. Chen, G.A. Thouas. **Metallic implant biomaterials.** Mater. Sci. Eng.: R: Rep., 87 (2015), pp. 1-57

[7] C. Ng, O. Chan, H. Man. **Formation of TiN grid on NiTi by laser gas nitriding for improving wear resistance in Hanks' solution.** J. Mater. Sci. Technol., 32 (2016), pp. 459-464

[8] V. Jain, M. Lykissas, P. Trobisch, E. Wall, P. Newton, P. Sturm, P. Cahill, D. Bylski-Austrow. **Surgical aspects of spinal growth modulation in scoliosis correction.** Instr. Course Lect., 63 (2014), pp. 335-344

[9] M. Seong, K. Mohanchandra, Y. Lin, G.P. Carman. **Development of a 'bi-layer lift-off'method for high flow rate and high frequency Nitinol MEMS valve fabrication.** J. Micromech. Microeng., 18 (2008), Article 075034

[10]M. Simon, C.A. Athanasoulis, D. Kim, F.L. Steinberg, D. Porter, B. Byse, S. Kleshinski, S. Geller, D. Orr on, A. Waltman. **Simon nitinol inferior vena cava filter: initial clinical experience. Work in progress.** Radiology, 172 (1989), pp. 99-103

[11] P. Sobieszczyk. **Factors to consider regarding the need for inferior vena cava filters.** Prog. Cardiovasc. Dis., 60 (2018), pp. 622-628

[12] H.-H. Huang, Y.-H. Chiu, T.-H. Lee, S.-C. Wu, H.-W. Yang, K.-H. Su, C.-C. Hsu. **Ion release from NiTi orthodontic wires in artificial saliva with various acidities.** Biomaterials, 24 (2003), pp. 3585-3592

[13]R.R. Saxon, A. Chervu, P.A. Jones, T.K. Bajwa, D.R. Gable, P.A. Soukas, R.J. Begg, J.G. Adams, G.M. A nsel, D.B. Schneider. **Heparin-bonded, expanded polytetrafluoroethylene-lined stent graft in the treatment of femoropopliteal artery disease: 1-year results of the VIPER (viabahn endoprosthesis with heparin bioactive surface in the treatment of superficial femoral artery obstructive disease) trial.** J. Vasc. Interv. Radiol., 24 (2013), pp. 165-173

[14] D. Tsetis, R. Uberoi. **Quality improvement guidelines for endovascular treatment of iliac artery occlusive disease.** Cardiovasc. Intervent. Radiol., 31 (2008), pp. 238-245

[15] V. Videm, A. Ødegård, H.O. Myhre. **Iohexol-induced neutrophil myeloperoxidase release and activation upon contact with vascular stent-graft material: a mechanism contributing to the postimplantation syndrome?** J. Endovasc. Therapy, 10 (2003), pp. 958-967

[16] G. Wang, S. Moya, Z. Lu, D. Gregurec, H. Zreiqat. **Enhancing orthopedic implant bioactivity: refining the nanotopography.** Nanomedicine, 10 (2015), pp. 1327-1341

[17] N. Wang, D. Xiong. **Superhydrophobic membranes on metal substrate and their corrosion protection in different corrosive media.** Appl. Surf. Sci., 305 (2014), pp. 603-608

[18] R. Blossey. **Self-cleaning surfaces—virtual realities.** Nat. Mater., 2 (2003), pp. 301-306

[19] X. Feng, Y. Zhang, G. Wang, M. Miao, L. Shi. **Dual-surface modification of calcium sulfate whisker with sodium hexametaphosphate/silica and use as new water-resistant reinforcing fillers in papermaking.** Powder Technol., 271 (2015), pp. 1-6

[20] P. Brown, O. Atkinson, J. Badyal. **Ultrafast oleophobic–hydrophilic switching surfaces for antifogging, self-cleaning, and oil–water separation.** ACS Appl. Mater. Interfaces, 6 (2014), pp. 7504-7511

[21] S. Zhang, J. Huang, Y. Cheng, H. Yang, Z. Chen, Y. Lai. **Bioinspired surfaces with superwettability for anti-icing and ice-phobic application: concept mechanism, and design.** Small, 13 (2017), p. 1701867

[22] T. Xiang, Y. Han, Z. Guo, R. Wang, S. Zheng, S. Li, C. Li, X. Dai. **Fabrication of inherent anticorrosion superhydrophobic surfaces on metals.** ACS Sustain. Chem. Eng., 6 (2018), pp. 5598-5606

[23] K. Watanabe, Y. Udagawa, H. Udagawa. **Drag reduction of Newtonian fluid in a circular pipe with a highly water-repellent wall.** J. Fluid Mech., 381 (1999), pp. 225-238

[24] M. Shaker, E. Salahinejad. **A combined criterion of surface free energy and roughness to predict the wettability of non-ideal low-energy surfaces.** Prog. Org. Coat., 119 (2018), pp. 123-126

[25] C. Wu, J. Chang. **Synthesis and apatite-formation ability of akermanite.** Mater. Lett., 58 (2004), pp. 2415-2417

[26] T. Sun, L. Feng, X. Gao, L. Jiang. **Bioinspired surfaces with special wettability.** Acc. Chem. Res., 38 (2005), pp. 644-652

[27] Y. Lai, J. Huang, Z. Cui, M. Ge, K.Q. Zhang, Z. Chen, L. Chi. **Recent advances in TiO2-based nanostructured surfaces with controllable wettability and adhesion.** Small, 12 (2016), pp. 2203-2224

[28] Y. Lai, L. Lin, F. Pan, J. Huang, R. Song, Y. Huang, C. Lin, H. Fuchs, L. Chi. **Bioinspired patterning with extreme wettability contrast on TiO2 nanotube array surface: a versatile platform for biomedical applications.** Small, 9 (2013), pp. 2945-2953

[29] J. Li, G. Wang, D. Wang, Q. Wu, X. Jiang, X. Liu. **Alkali-treated titanium selectively regulating biological behaviors of bacteria, cancer cells and mesenchymal stem cells.** J. Colloid Interface Sci., 436 (2014), pp. 160-170

[30] L. Xu, W. Zhuang, B. Xu, Z. Cai. **Fabrication of superhydrophobic cotton fabrics by silica hydrosol and hydrophobization.** Appl. Surf. Sci., 257 (2011), pp. 5491-5498

[31] M. Shaker, E. Salahinejad, F. Ashtari-Mahini. **Hydrophobization of metallic surfaces by means of Al2O3-HDTMS coatings.** Appl. Surf. Sci., 428 (2018), pp. 455-462

[32] Q. Gao, Q. Zhu, Y. Guo, C.Q. Yang. **Formation of highly hydrophobic surfaces on cotton and polyester fabrics using silica sol nanoparticles and nonfluorinated alkylsilane.** Ind. Eng. Chem. Res., 48 (2009), pp. 9797-9803

[33] N. Gao, M. Li, W. Jing, Y. Fan, N. Xu. **Improving the filtration performance of ZrO2 membrane in non-polar organic solvents by surface hydrophobic modification.** J. Membr. Sci., 375 (2011), pp. 276-283

[34] M. Textor, C. Sittig, V. Frauchiger, S. Tosatti, D.M. Brunette. **Properties and biological significance of natural oxide films on titanium and its alloys.** Titanium in Medicine, Springer (2001), pp. 171-230

[35] S. Rastegari, E. Salahinejad. **Surface modification of Ti-6Al-4V alloy for osseointegration by alkaline treatment and chitosan-matrix glass-reinforced nanocomposite coating.** Carbohydr. Polym., 205 (2019), pp. 302-311

[36] J. Katić, M. Metikoš-Huković, S.D. Škapin, M. Petravić, M. Varašanec. **The potential-assisted deposition as valuable tool for producing functional apatite coatings on metallic materials.** Electrochim. Acta, 127 (2014), pp. 173-179

[37] A. Sepahvandi, F. Moztarzadeh, M. Mozafari, M. Ghaffari, N. Raee. **Photoluminescence in the characterization and early detection of biomimetic bone-like apatite formation on the surface of alkaline-treated titanium implant: State of the art.** Colloids Surf., B, 86 (2011), pp. 390-396

[38] L. Jonášová, F.A. Müller, A. Helebrant, J. Strnad, P. Greil. **Biomimetic apatite formation on chemically treated titanium.** Biomaterials, 25 (2004), pp. 1187-1194

[39] S. Karimi, E. Salahinejad, E. Sharifi, A. Nourian, L. Tayebi. **Bioperformance of chitosan/fluoride-doped diopside nanocomposite coatings deposited on medical stainless steel.** Carbohydr. Polym., 202 (2018), pp. 600-610

[40] W. Yuan, Y. Feng, H. Wang, D. Yang, B. An, W. Zhang, M. Khan, J. Guo. **Hemocompatible surface of electrospun nanofibrous scaffolds by ATRP modification.** Mater. Sci. Eng., C, 33 (2013), pp. 3644-3651

[41] J. Zhang, A. Deng, Y. Yang, L. Gao, N. Xu, X. Liu, L. Hu, J. Chen, S. Yang. **HPLC detection of loss rate and cell migration of HUVECs in a proanthocyanidin cross-linked recombinant human collagen-peptide (RHC)–chitosan scaffold.** Mater. Sci. Eng., C, 56 (2015), pp. 555-563

[42] H. Goodarzi, K. Jadidi, S. Pourmotabed, E. Sharifi, H. Aghamollaei. **Preparation and in vitro characterization of cross-linked collagen–gelatin hydrogel using EDC/NHS for corneal tissue engineering applications.** Int. J. Biol. Macromol., 126 (2019), pp. 620-632

[43] X. Rao, C. Chu, C.Y. Chung, P.K. Chu. **Hydrothermal growth mechanism of controllable hydrophilic titanate nanostructures on medical NiTi shape memory alloy.** J. Mater. Eng. Perform., 21 (2012), pp. 2600-2606

[44] C. Sekhar, B. Roy, S. Aich. **Synthesis of nanoscale oxide scaffold on Nitinol surface using hydrothermal treatment.** Surf. Eng., 31 (2015), pp. 747-751

[45] S. Wu, X. Liu, T. Hu, P.K. Chu, J. Ho, Y. Chan, K. Yeung, C. Chu, T. Hung, K. Huo. **A biomimetic hierarchical scaffold: natural growth of nanotitanates on three-dimensional microporous Ti-based metals.** Nano Lett., 8 (2008), pp. 3803-3808

[46] S. Koonaphapdeelert, K. Li. **Preparation and characterization of hydrophobic ceramic hollow fibre membrane.** J. Membr. Sci., 291 (2007), pp. 70-76

[47] X. Yang, R. Hu, S. Zhu, C. Li, M. Chen, L. Zhang, Z. Cui. **Accelerating the formation of a calcium phosphate layer on NiTi alloy by chemical treatments.** Scr. Mater., 54 (2006), pp. 1457-1462

[48] C.W. Lai, S.B.A. Hamid, T.L. Tan, W.H. Lee. **Rapid formation of 1D titanate nanotubes using alkaline hydrothermal treatment and its photocatalytic performance.** J. Nanomater., 2015 (2015), pp. 1-7

[49] H.M. Kim, F. Miyaji, T. Kokubo, S. Nishiguchi, T. Nakamura. **Graded surface structure of bioactive titanium prepared by chemical treatment.** J. Biomed. Mater. Res., 45 (1999), pp. 100-107

[50] C. Chu, C. Chung, Y. Pu, P. Lin. **Graded surface structure in chemically polished NiTi shape memory alloy after NaOH treatment.** Scr. Mater., 52 (2005), pp. 1117-1121

[51] H.M. Kim, F. Miyaji, T. Kokubo, T. Nakamura. **Preparation of bioactive Ti and its alloys via simple chemical surface treatment.** J. Biomed. Mater. Res., 32 (1996), pp. 409-417

[52] X. Lu, Y. Wang, X. Yang, Q. Zhang, Z. Zhao, L.T. Weng, Y. Leng. **Spectroscopic analysis of titanium surface functional groups under various surface modification and their behaviors in vitro and in vivo.** J. Biomed. Mater. Res. Part A, 84 (2008), pp. 523-534

[53] A. Shukla, R. Balasubramaniam. **Effect of surface treatment on electrochemical behavior of CP Ti, Ti–6Al–4V and Ti–13Nb–13Zr alloys in simulated human body fluid.** Corros. Sci., 48 (2006), pp. 1696-1720

[54] R.N. Wenzel. **Resistance of solid surfaces to wetting by water.** Ind. Eng. Chem., 28 (1936), pp. 988-994

[55] A. Cassie, S. Baxter. **Wettability of porous surfaces.** Trans. Faraday Soc., 40 (1944), pp. 546-551

[56] D. Quéré. **Surface chemistry: Fakir droplets.** Nat. Mater., 1 (2002), pp. 14-15

[57] K.K. Lau, J. Bico, K.B. Teo, M. Chhowalla, G.A. Amaratunga, W.I. Milne, G.H. McKinley, K.K. Gleason. **Superhydrophobic carbon nanotube forests.** Nano Lett., 3 (2003), pp. 1701-1705

[58] J. Huser, S. Bistac, M. Brogly, C. Delaite, T. Lasuye, B. Stasik. **Investigation on the adsorption of alkoxysilanes on stainless steel.** Appl. Spectrosc., 67 (2013), pp. 1308-1314

[59] S. Rossi, F. Deflorian, A. Pegoretti, D. D'Orazio, S. Gialanella. **Chemical and mechanical treatments to improve the surface properties of shape memory NiTi wires.** Surf. Coat. Technol., 202 (2008), pp. 2214-2222

[60] F. Zucchi, V. Grassi, A. Frignani, C. Monticelli, G. Trabanelli. **Electrochemical behaviour of a magnesium alloy containing rare earth elements.** J. Appl. Electrochem., 36 (2006), pp. 195-204

[61] H. Cesiulis, N. Tsyntsaru, A. Ramanavicius, G. Ragoisha. **The study of thin films by electrochemical impedance spectroscopy.** Nanostructures and thin films for multifunctional applications, Springer (2016)

[62] A.J. Bard, L.R. Faulkner. **Electrochemical methods: Fundamentals and applications.** John Wiley & Sons Inc (2001)

[63] J. Sui, Z. Gao, W. Cai, Z. Zhang. **Corrosion behavior of NiTi alloys coated with diamond-like carbon (DLC) fabricated by plasma immersion ion implantation and deposition.** Mater. Sci. Eng., A, 452 (2007), pp. 518-523

[64] A.-S. Andersson, J. Brink, U. Lidberg, D.S. Sutherland. **Influence of systematically varied nanoscale topography on the morphology of epithelial cells.** IEEE Trans. Nanobiosci., 2 (2003), pp. 49-57

[65] M.J. Dalby, N. Gadegaard, R. Tare, A. Andar, M.O. Riehle, P. Herzyk, C.D. Wilkinson, R.O. Oreffo. **The control of human mesenchymal cell differentiation using nanoscale symmetry and disorder.** Nat. Mater., 6 (2007), pp. 997-1003

[66] M. Karlsson, L. Tang. **Surface morphology and adsorbed proteins affect phagocyte responses to nano-porous alumina.** J. Mater. Sci. - Mater. Med., 17 (2006), pp. 1101-1111

[67] M.J. Dalby, N. Gadegaard, P. Herzyk, H. Agheli, D.S. Sutherland, C.D. Wilkinson. **Group analysis of regulation of fibroblast genome on low-adhesion nanostructures.** Biomaterials, 28 (2007), pp. 1761-1769

[68] W.-Q. Yan, T. Nakamura, K. Kawanabe, S. Nishigochi, M. Oka, T. Kokubo. **Apatite layer-coated titanium for use as bone bonding implants.** Biomaterials, 18 (1997), pp. 1185-1190

[69] J. Brash. **Hydrophobic polymer surfaces and their interactions with blood.** Ann. N. Y. Acad. Sci., 283 (1977), pp. 356-371